



Article

The Ocean Surface Current in the East China Sea Computed by the Geostationary Ocean Color Imager Satellite

Youzhi Ma ¹, Wenbin Yin ^{1,*} , Zheng Guo ¹ and Jiliang Xuan ²¹ College of Marine Science and Technology, Zhejiang Ocean University, Zhoushan 316022, China² State Key Laboratory of Satellite Ocean Environment Dynamics, Second Institute of Oceanography, Ministry of Natural Resources, Hangzhou 310012, China

* Correspondence: yinwenbin@zjou.edu.cn

Abstract: High-frequency observations of surface current field data over large areas and long time series are imperative for comprehending sea-air interaction and ocean dynamics. Nonetheless, neither in situ observations nor polar-orbiting satellites can fulfill the requirements necessary for such observations. In recent years, geostationary satellite data with ultra-high temporal resolution have been increasingly utilized for the computation of surface flow fields. In this paper, the surface flow field in the East China Sea is estimated using maximum cross-correlation, which is the most widely used flow field computation algorithm, based on the total suspended solids (TSS) data acquired from the Geostationary Ocean Color Imager satellite. The inversion results were compared with the modeled tidal current data and the measured tidal elevation data for verification. The results of the verification demonstrated that the mean deviation of the long semiaxis of the tidal ellipse of the inverted M_2 tide is 0.0335 m/s, the mean deviation of the short semiaxis is 0.0276 m/s, and the mean deviation of the tilt angle is 6.89° . Moreover, the spatially averaged flow velocity corresponds with the observed pattern of tidal elevation changes, thus showcasing the field's significant reliability. Afterward, we calculated the sea surface current fields in the East China Sea for the years 2013 to 2019 and created distribution maps for both climatology and seasonality. The resulting current charts provide an intuitive display of the spatial structure and seasonal variations in the East China Sea circulation. Lastly, we performed a diagnostic analysis on the surface TSS variation mechanism in the frontal zone along the Zhejiang coast, utilizing inverted flow data collected on 3 August 2013, which had a high spatial coverage and complete time series. Our analysis revealed that the intraday variation in TSS in the local surface layer was primarily influenced by tide-induced vertical mixing. The research findings of this article not only provide valuable data support for the study of local ocean dynamics but also verify the reliability of short-period surface flow inversion of high-turbidity waters near the coast using geostationary satellites.

Keywords: East China Sea; surface current; MCC; GOCI; TSS; intraday variation

Citation: Ma, Y.; Yin, W.; Guo, Z.; Xuan, J. The Ocean Surface Current in the East China Sea Computed by the Geostationary Ocean Color Imager Satellite. *Remote Sens.* **2023**, *15*, 2210. <https://doi.org/10.3390/rs15082210>

Academic Editor: Yukiharu Hisaki

Received: 27 March 2023

Revised: 18 April 2023

Accepted: 20 April 2023

Published: 21 April 2023



Copyright: © 2023 by the authors. Licensee MDPI, Basel, Switzerland. This article is an open access article distributed under the terms and conditions of the Creative Commons Attribution (CC BY) license (<https://creativecommons.org/licenses/by/4.0/>).

1. Introduction

Oceanic currents represent a crucial type of seawater flow, delineating the extensive and relatively steady motion of water masses. These currents assume a pivotal function in the conveyance and repositioning of oceanic energy and substances. Consequently, monitoring ocean currents holds paramount significance in maritime transportation, production, disaster mitigation, and rescue efforts, as well as scientific investigations. Of the traditional methods for observing flow fields, in situ observation data are renowned for their high accuracy and reliability, but their high cost of observation presents a challenge. While drifting buoys are capable of continuously monitoring the surrounding currents, their passive motion trajectory renders them incapable of capturing a large area flow field [1]. Although high-frequency ground wave radar [2] offers precise observation, its widespread use is hindered by the associated costs of deployment and maintenance and its observation

range is limited to within 180 km of the shoreline. The sea surface height data of the satellite altimeter [3] can be used to calculate the mesoscale geostrophic flow; however, the impact of land pollution and atmospheric errors can result in significant errors in observations near the shore. Moreover, its spatial resolution of $1/4^\circ$ is inadequate for submesoscale studies.

The utilization of satellite remote-sensing technology for the inversion of large-scale sea surface flow fields is progressively increasing as it can acquire sea surface data on a large scale simultaneously. Emery [4] developed a feature tracking method based on continuous satellite remote-sensing imagery—the maximum cross-correlation (MCC) algorithm. With the use of advanced very-high-resolution radiometry (AVHRR) SST data, he successfully inferred the flow field of the coastal waters of British Columbia, revealing the great potential of remote-sensing imagery for the inference of sea surface flow fields. Since then, this algorithm has become one of the most widely applied methods for satellite inference of sea surface flow fields. Tokmakian [5] calculated the daily ocean surface currents near California using continuous images captured by the coastal zone color scanner (CZCS) and AVHRR and then compared the results with acoustic Doppler current profiler (ADCP) measurement data. The comparison revealed an RMSE of 0.14–0.25 m/s. Through the utilization of the MCC algorithm, Bowen [6] extracted a time series of flow fields from AVHRR data for the East Australian Current, encompassing a period of 7 years (1993–1999). The precision of the estimation is estimated to be between 0.08 and 0.2 m/s RMS. The mean flow, time-varying flow, and eddy kinetic energy derived from the time series were compared with observations and demonstrated similar characteristics. Crocker [7] used a moderate-resolution imaging spectroradiometer (MODIS) and sea-viewing wide field-of-view sensor (SeaWiFS) ocean color imagery at a resolution of 1.1 km to calculate the sea surface flow field of the central California Current, in order to investigate the potential for supplementing the MCC currents derived from thermal AVHRR imagery. The results indicate a strong agreement between the two velocity products, with a mean correlation of 0.74, a mean RMS difference of 7.4 cm/s, and a mean bias of less than 2 cm/s, which is considerably smaller than the established absolute error of the MCC method. By merging the thermal and ocean color MCC velocity fields, the spatial coverage for this specific case study is increased by approximately 25%.

Despite the good performance of polar-orbiting satellite products in the aforementioned studies on sea surface flow inversion, there are still significant drawbacks. In areas with complex circulation patterns, particularly in coastal regions dominated by tidal currents, the temporal resolution of polar-orbiting satellites is insufficient to capture short-term water movements. In contrast to polar-orbiting satellites, which typically revisit a given location on Earth no more frequently than every 12 or 24 h, geostationary satellites remain stationary above a fixed point on the Earth's surface for prolonged periods. This allows for uninterrupted observation of specific areas, providing distinct advantages in remote-sensing monitoring of highly dynamic and hydrodynamic environments. As a result, geostationary satellites are increasingly being used to study intraday high-frequency variations in the sea surface flow field. Yang [8] computed the flow field at the ocean surface by utilizing eight Geostationary Ocean Color Imager (GOCI)-derived total suspended solids (TSS) images from highly turbid coastal waters, as well as images of chlorophyll concentration for relatively clear waters. The findings indicated that GOCI TSS-derived ocean surface currents can effectively estimate and represent fast tidal currents, as well as flood and ebb tides along the western coast of Korea, as compared to in situ measurements. Furthermore, GOCI-derived CHL scenes successfully depicted currents along boundaries where warm and cold seawaters mix, as well as mesoscale currents such as the East Korea Warm Current in the East Sea of Korea. Based on GOCI's unique 8-hourly local daytime sequential TSS images, Hu [9] has produced a depiction of the semidiurnal M_2 tidal currents in the East China Sea (ECS). The derived results demonstrate good consistency with observations from a comprehensive set of twenty-eight surface drifters and four mooring instruments, as well as with the high-resolution regional tidal model data from Oregon State University. Based on the hourly SST data obtained from the Himawari-8 satellite, Taniguchi [10] employed

the MCC algorithm to analyze the short-term surface flow variations in the area south of the Lombok Strait during the northern summer. The findings indicate a southward flow from the Lombok Strait to the Indian Ocean, hindering the eastward movement of the South Java Current along the northern summer and the Java Current along the southern coast of Nusa Tenggara. Zhu [11] utilized the 10 min data from the Himawari-8 satellite to retrieve the coastal currents in Hangzhou Bay. The comparative analysis with the numerical model data from the Taiwan Strait current forecasting system demonstrates that the Himawari-8 satellite data can be efficaciously employed for the precise estimation of oceanic currents.

The aforementioned study demonstrates the exceptional performance of geostationary satellite products in inverting the short-period variation process of the sea surface current field. Consequently, this paper uses the hourly TSS images of GOCI to invert the sea surface current field in the ECS (Figure 1). Subsequently, through diagnostic analysis, we aim to investigate the primary mechanisms that impact the intraday variation in the sea surface TSS in the frontal zone along the coast of Zhejiang. The Zhejiang offshore is situated on the southeastern coast of China, on the western part of the ECS shelf. The water masses are composed of offshore water masses dominated by the Taiwan Warm Current (TWC) and nearshore water masses dominated by the Zhejiang Coastal Current (ZJCC). The boundary between these two water masses forms the Zhejiang Coastal Front (ZJCF), which is created due to significant differences in their hydrological properties. The dynamic environment in the front zone is complex and variable due to various factors such as terrestrial runoff, tides, monsoons, and solar radiation. Consequently, the spatial distribution of TSS in this region is complex and undergoes high-frequency changes [12,13]. The objective of this article is not solely to furnish valuable data support for investigating the local ocean dynamics but also to authenticate the dependability of short-period surface flow inversion in high-turbidity waters in close proximity to the coast through the employment of geostationary satellites. Section 2 presents a comprehensive summary of the data and methods utilized in this study. Section 3, which encompasses the Results and Discussion, exhibits the validation outcomes of the GOCI-derived flow field and scrutinizes the mean flow in the East China Sea. Building upon this foundation, it explores the diurnal variation characteristics and dominant mechanisms of TSS in the frontal zone along the coast of Zhejiang. The conclusions of the study are summarized in Section 4.

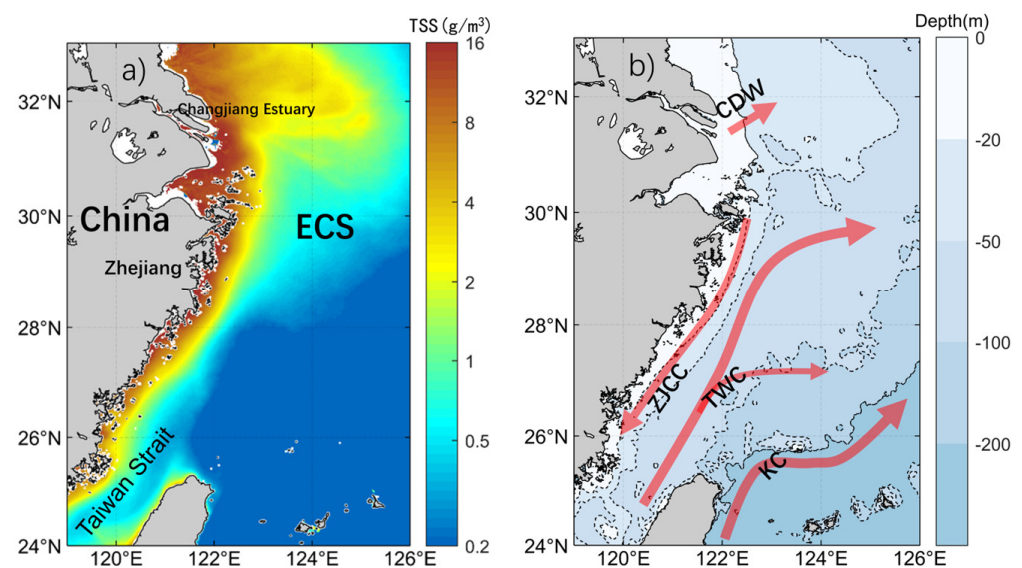


Figure 1. (a) Spatial distribution of GOCI climatological TSS in the East China Sea; (b) the schematic diagram of ocean circulation (the background color in (b) is the water depth). **KC:** Kuroshio Current; **TWC:** Taiwan Warm Current; **CDW:** Changjiang Diluted Water; **ZJCC:** Zhejiang Coastal Current.

2. Data and Methods

2.1. Data

2.1.1. GOCI TSS Data

The selection of a tracer has a momentous influence on the inversion performance of the MCC algorithm. Opting for temperature as a tracer often neglects the flow along isotherms in the ocean. Hence, we utilized the level-2 ocean color data TSS obtained from the geostationary orbit satellite GOCI [14] for the period spanning 2013–2019 to invert the surface flow field of the East China Sea. GOCI, short for Geostationary Ocean Color Imager, is the world's first geostationary orbit ocean color satellite sensor, belonging to the Korea Ocean Satellite Center (KOSC). It was launched on 27 June 2010, on board the Korean geostationary meteorological satellite, the communication, ocean, and meteorological satellite (COMS), with a designed lifespan of about 7.7 years. GOCI has six visible bands and two near-infrared bands and can observe an area of $2500 \text{ km} \times 2500 \text{ km}$ centered at 130°E longitude and 36°N latitude. The spatial resolution of GOCI is 500 m, with eight daily observations of the ground and a one-hour observation interval spanning from 8:16 to 15:45 Beijing time. Compared with polar orbit ocean color satellites, GOCI can continuously observe changes in ocean color information from a stationary satellite platform, achieving high temporal and spatial resolution for Earth observation. This capability contributes to the study of complex and rapidly changing short-period dynamic processes in the ocean. GOCI data were downloaded from the KOSC website (<https://kosc.kiost.ac.kr/>, accessed on 23 December 2021). After the data download was completed, it was necessary to conduct a manual screening to identify continuous cloud-free or less-cloudy images of the study area. Theoretically, up to eight continuous cloud-free or less-cloudy images can be obtained for one day. As a result, a maximum of seven consecutive flow maps can be inverted. After the manual screening, the selected GOCI TSS data was subjected to a 5×5 median filter to eliminate remote-sensing image noise [15].

2.1.2. Tide Data

The dataset employed for validating the inverse flow field comprises finite-volume community ocean model (FVCOM) data from Xuan [16]. Notably, the M_2 tidal constituent exhibits consistency with the co-tidal chart obtained from 10 years of satellite measurements and coastal island station observations. The numerical simulation results impeccably replicate the tidal flow field in the coastal regions of Zhejiang.

To derive the residual tidal current field in the ECS, it is necessary to remove the concurrent tidal current data from the inverted flow field. In this study, the tidal current data utilized was sourced from TPXO8, a globally implemented framework constructed by Oregon State University. TPXO8 [17] utilizes two-dimensional barotropic fluid equations and generalized inversion methods to assimilate measured data and provides a comprehensive range of information on the amplitudes and phases of various tidal components. These include the eight main tidal components, two long-period tidal components (M_f and M_m), three shallow-water tidal components (M_4 , MS_4 , and MN_4), as well as $2N_2$, S_1 , and other additional tidal components. The data can be downloaded from the website (<https://www.tpxo.net/global/tpxo8-atlas>, accessed on 15 December 2022).

2.2. Method

2.2.1. Maximum Cross-Correlation (MCC) Algorithm

The algorithm utilized in this study for inverting ocean surface currents is the widely used maximum cross-correlation (MCC) method, which was proposed by Emery in 1986 as a Lagrangian method for computing ocean currents. Its principle involves calculating the cross-correlation coefficient of two remote-sensing images from adjacent time periods, identifying the maximum coefficient to determine the displacement information of a water mass between the two time periods, and dividing it by the time interval to obtain the flow velocity. The specific steps of this procedure are depicted in Figure 2.

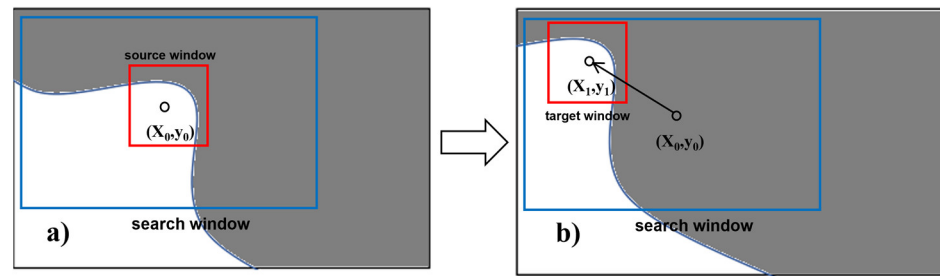


Figure 2. Two consecutive remote-sensing image images T_0 (a) and T_1 (b), used for calculating the cross-correlation coefficient of the source window (red square) and the target window in the search window (blue square) to search for the position of the highest cross-correlation value and to obtain the velocity vector.

Given remote-sensing images at two adjacent time points, denoted as T_0 and T_1 , with a time interval of Δt , a square source window with a center (X_0, Y_0) and radius r is selected in the image T_0 . Next, a square search window with a center (X_0, Y_0) and a larger side length R ($R > r$) is chosen in the image T_1 . Within the search window, similarly sized target windows are sequentially selected, and the cross-correlation coefficient (CC) between the source window and each target window is calculated. The formula for computing CC is as follows [4]:

$$CC = \frac{\sum_{i=1}^{i=2r+1} \sum_{j=1}^{j=2r+1} (S_S(i, j) - \bar{S}_S) (S_T(i, j) - \bar{S}_T)}{\sqrt{\sum_{i=1}^{i=2r+1} \sum_{j=1}^{j=2r+1} (S_S(i, j) - \bar{S}_S)^2 \sum_{i=1}^{i=2r+1} \sum_{j=1}^{j=2r+1} (S_T(i, j) - \bar{S}_T)^2}} \quad (1)$$

Here, $S_S(i, j)$ and $S_T(i, j)$ denote the TSS values at the i -th row and j -th column within the source window and the target window, respectively. \bar{S}_S and \bar{S}_T represent the average TSS values within the source window and the target window, respectively.

By applying the aforementioned formula, we obtained the correlation coefficient values between all target windows and the source window. Based on previous studies, the threshold for the cross-correlation coefficient CC is set at 0.9 [18]. This means that target windows with a CC value less than 0.9 are considered irrelevant to the source window. After that, the target window with the highest value CC_{max} was identified as the position of the source window at a time T_1 , with its central position at (X_1, Y_1) . The horizontal displacement of the source window ΔL within the time interval Δt is calculated as $\Delta L = \sqrt{(X_1 - X_0)^2 + (Y_1 - Y_0)^2}$. The horizontal velocity of the water mass, which is equivalent to the flow speed V and direction θ of the ocean current at that location, can be calculated as:

$$V = \frac{\Delta L}{\Delta t} \quad (2)$$

$$\theta = \tan^{-1} \frac{Y_1 - Y_0}{X_1 - X_0} \quad (3)$$

Using the above method, source windows are selected in the T_0 image one by one, and the flow velocity is calculated using the MCC algorithm. After summarizing the results, a large-scale synchronized flow field of the surface layer of the studied sea area can be obtained. Referring to previous studies [19], the inverted flow field needs to be filtered using correlation coefficient thresholding, reciprocal filtering, and neighborhood vector averaging to eliminate spurious flow velocity vectors.

2.2.2. Selection of the Radius r for the Source Window

The selection of radii for both the source and search windows can significantly affect the effective data quantity and accuracy of the inversion results. According to Du [20], the radius of the search window has little effect on the inversion performance of the MCC

algorithm. Therefore, this study aims to investigate the impact of the source window radius (r) on the inversion of the flow field to determine the optimal value of r . The size of the search window only needs to be large enough to include the expected maximum flow velocity in the study area. Based on historical data, the search window radius (R) is set to $r+8$ in this study.

To determine the optimal source window radius r , a series of experiments were conducted in this study. The values of r were tested incrementally from 5 to 20, and the resulting surface flow fields were computed and subjected to harmonic analysis to derive the M_2 tidal ellipse. Subsequently, the root-mean-square error of the long and short axes and inclination angle of the M_2 tidal ellipse of the inverted flow field were calculated using the simulated M_2 tidal ellipse of the flow field as a reference. The experimental results (see Figure 3) showed a decrease in the root-mean-square errors of the long and short axes and inclination angle with an increase in r . Notably, the inclination angle error reached a significant minimum at $r = 17$. Although the inversion error continued to decrease for r values greater than 20, the rate of decrease had slowed down. Hence, considering the efficiency and accuracy of the inversion algorithm, we concluded that the optimal value of r for the source window radius is 17.

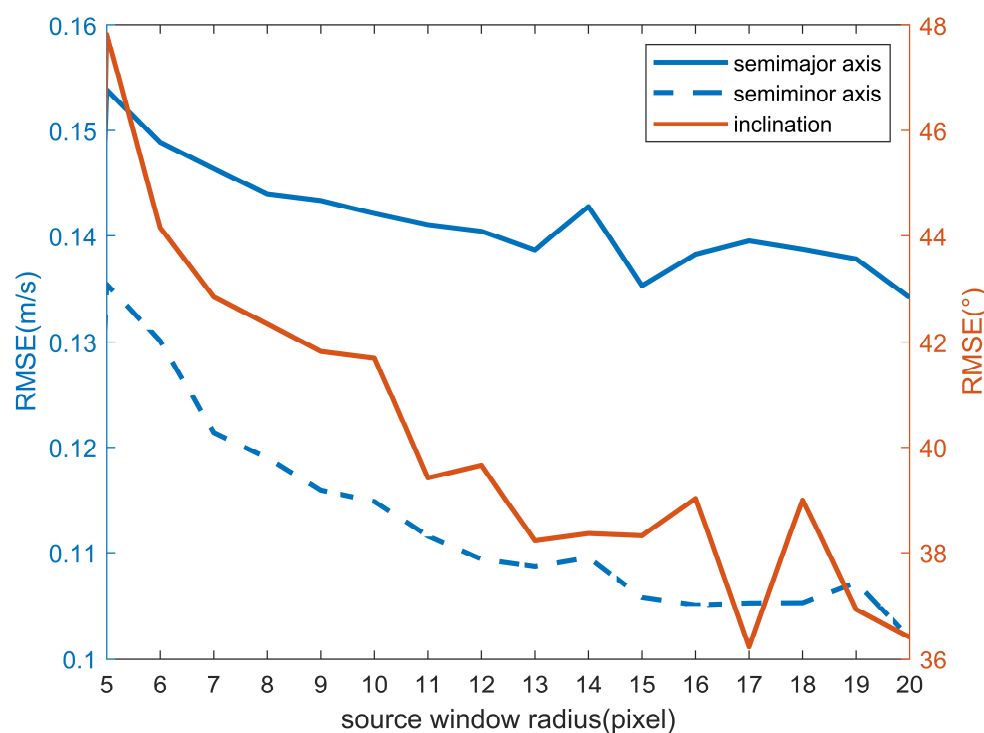


Figure 3. The RMSE of semimajor (solid blue line), semiminor (blue dotted line) axis, and inclination (solid red line) under different source window radius r .

3. Results and Discussion

3.1. Verification of Inversion Results Based on Numerical Modeling and In Situ Measurements

To verify the accuracy of the inverted flow field, we initially conducted a harmonic analysis of the inverted flow field dataset and derived the tidal ellipse for the M_2 constituent. The dependability of the MCC inverted flow field was evaluated by comparing the tidal ellipses of the inverted flow field and the model flow field and calculating the root-mean-square error of the long and short axes, and the inclination angle between the two. The comparative results reveal that the M_2 tidal ellipses of the inverted flow field and the model flow field exhibit substantial consistency in the sea area south of the Yangtze River Estuary (Figure 4a). However, the consistency is comparatively poor in the Subei Shoal area. The calculated errors reveal that the average error of the long axis is 0.0335 m/s, the average error of the short axis is 0.0276 m/s, and the average error of the inclination

angle is 6.89° . Moreover, among the data points with good consistency, the accuracy in the shelf area is superior to that in the nearshore area, which might be attributable to the fact that the vertical sediment settling motion of nearshore water is more vigorous, and the variation in TSS is not dominated by the horizontal flow. We performed a spectrum analysis for one month's worth of tidal hourly elevation data, and the results (Figure 4b) showed two distinct peaks with frequencies of 2.2401×10^{-5} Hz and 2.3148×10^{-5} Hz, with a magnitude of 366.8782 and 102.1478, corresponding to periods of 12.4 h and 12.0 h. We consider that these two tidal components are M_2 and S_2 , which are the main components of tidal currents in the East China Sea and have a significant impact on the distribution of surface flow fields.

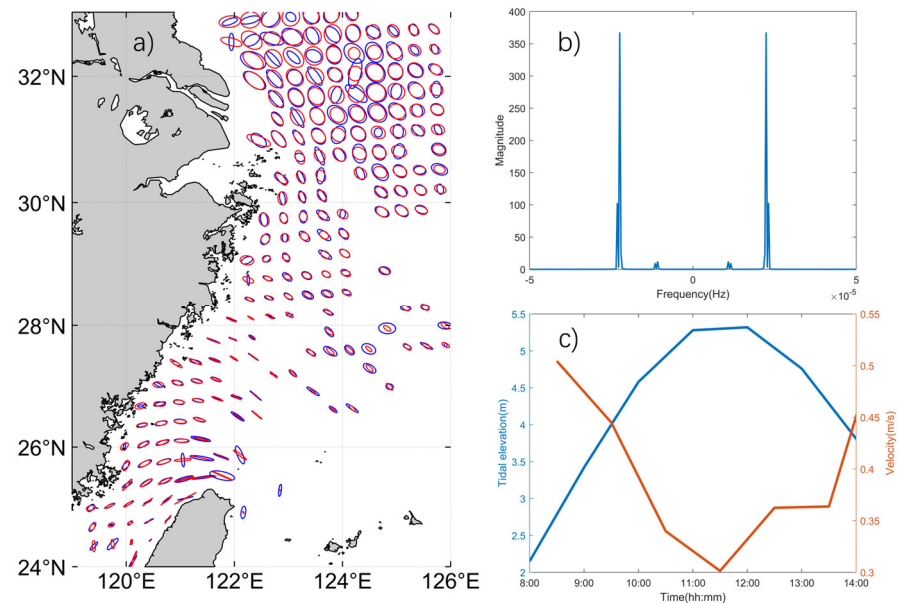


Figure 4. (a) M_2 tidal ellipse of MCC—derived current (blue) and the model flow (red), with a red star indicating the location of the local tide gauge station; (b) spectrum analysis of one month's worth of tidal hourly elevation data; and (c) tidal elevation variation and spatially averaged flow velocity on 14 February 2017.

In addition, we compared the mean flow velocity of the inverted flow field in the coastal area on 14 February 2017, using the observed tidal elevation changes measured at a local tide gauge station. The findings reveal that the two exhibit good synchronicity in their changes (Figure 4c). At the moment when the tidal elevation change was most drastic, the surface flow velocity also reached its maximum value. All of the above validation outcomes imply that the MCC algorithm in this study successfully inverts the ECS surface flow field, with good accuracy at different time scales, and can effectively represent the true flow conditions of the ECS surface water.

3.2. Pattern and Seasonal Variations of the Surface Residual Currents in the East China Sea

The comparative validation results demonstrate the reliability of the inverted flow field, thereby enabling analysis of circulation patterns and temporal variations in the ECS. To obtain the circulation patterns of the ECS, it is first necessary to remove the tidal current component from the inverted flow field. Therefore, we subtract the concurrently predicted tidal current data from TPX08 in the inverted flow field, and the remaining residual current field represents the circulation of the ECS. By following the aforementioned methodology, we acquired the residual flow data pertaining to the ECS during the period ranging from 2013 to 2019. Afterward, by averaging the obtained data, we were able to derive the climatological (Figure 5a) and seasonal (Figure 6a) circulation distribution maps of the ECS.

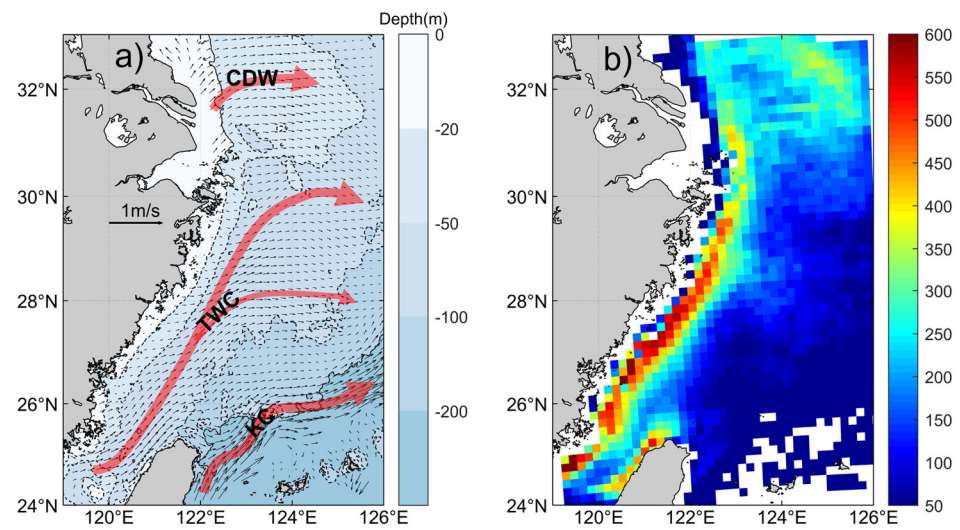


Figure 5. (a) GOCI-derived climatic current field; (b) spatial distribution of the number of velocity vectors in the flow field. KC: Kuroshio Current; TWC: Taiwan Warm Current; CDW: Changjiang Diluted Water. The red arrows in 5(a) show the trajectory of the currents.

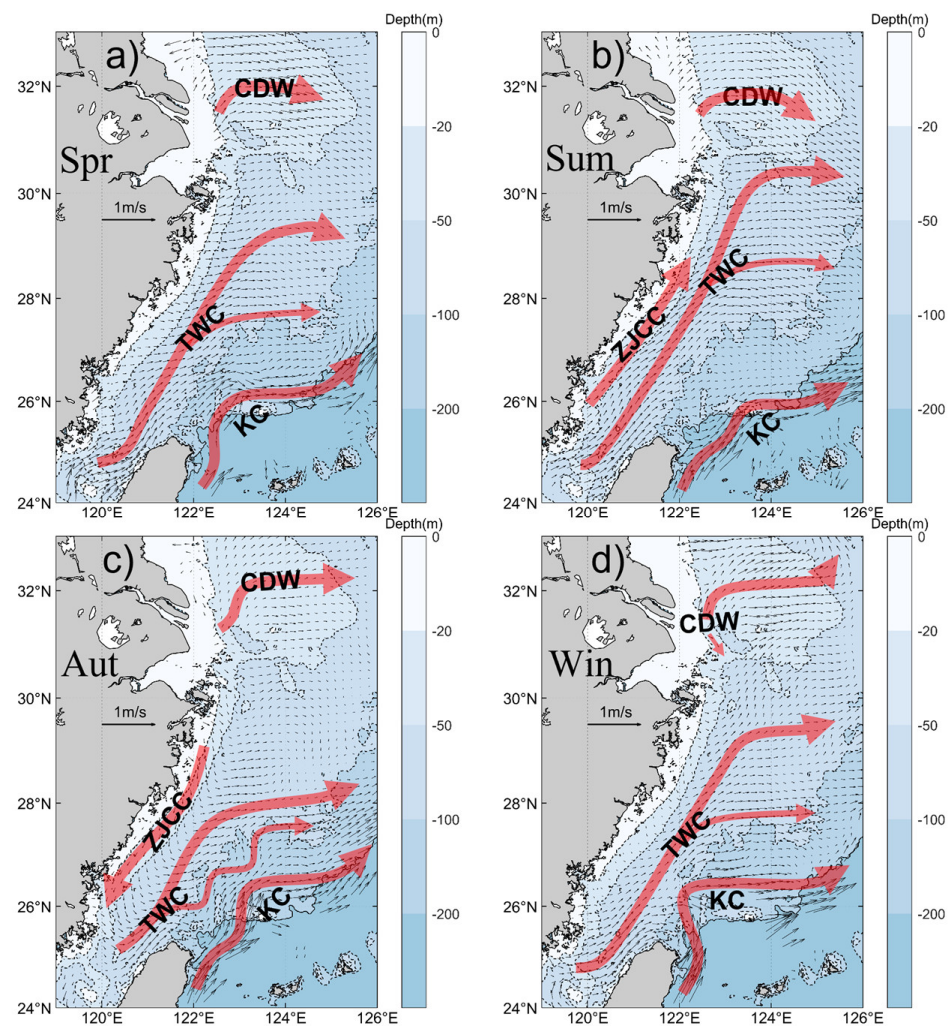


Figure 6. Seasonal surface mean flow in the East China Sea (red arrows indicate the main circulation). (a) Spring. (b) Summer. (c) Autumn. (d) Winter. KC: Kuroshio Current; TWC: Taiwan Warm Current; CDW: Changjiang Diluted Water; ZJCC: Zhejiang Coastal Current.

Figure 5a depicts the climatic flow field within the ECS, while Figure 5b portrays the spatial distribution of the number of velocity vectors that were utilized to compute the average. We can see that the quantity of velocity vectors is greater in the coastal regions of Zhejiang and Fujian provinces, as well as in the offshore zones situated in the western parts of Taiwan. This phenomenon can be chiefly ascribed to the heightened turbidity levels that prevail within these offshore areas, thereby rendering it more convenient for the algorithm to detect and track the motions of water masses. The sea surface flow field's climatic state divulges that the ECS's surface circulation is mainly composed of three prevailing current systems. The first current system, situated at the southeastern continental slope of the ECS, is the Kuroshio Current (KC), boasting the widest flow width and highest flow velocity [21]. It courses northwards along the eastern coast of Taiwan, enters the ECS at the northeastern part of Taiwan Island, and then takes a northeastward direction along the continental slope toward Japan. The KC's average velocity is approximately 0.86 m/s, and its maximum flow velocity can reach up to 1.42 m/s. As a robust western boundary current of the North Pacific, the KC exercises a significant influence on the circulation system of the ECS continental shelf area. The second oceanic current system is the Taiwan Warm Current (TWC), which flows northwards from the Taiwan Strait into the ECS throughout the year [22]. The TWC primarily moves northwards along the 50–100 m isobaths, with high-turbidity coastal waters on its left and low-turbidity continental shelf water masses on its right. Upon reaching 27°N, the TWC bifurcates into two branches, with one branch moving northwards along the coast and the other turning northeastwards to merge into the KC. The TWC significantly impacts the circulation structure of the nearshore regions of the western ECS. The third current system is the Changjiang Diluted Water (CDW), which carries a substantial amount of sediment and flows into the ECS from the Changjiang River estuary. It courses northeastward initially, then turns southeastward around 124°, and wields a crucial influence on the ecological and dynamic systems near the Changjiang River estuary [23].

Figures 6 and 7, respectively, showcase the seasonal variation in the inverted ECS surface current field and the seasonal distribution of the inverted sea current vector quantity. It is noticeable that the inverted sea current vector quantity from 2013 to 2019 exhibits significant seasonal differences: the summer season has the highest number of effective sea current vectors (Figure 7b) at 84,248; the winter season has the least at 32,765 (Figure 7d); while the spring and autumn seasons have 55,825 and 52,248 effective sea current vectors (Figure 7a,c), respectively. This indicates that besides the gradient magnitude of the selected tracer, cloud occlusion is also a major factor affecting the inversion performance of the MCC algorithm [24].

The seasonal distribution map of the reversed flow field exhibits pronounced seasonal fluctuations in the circulation system of the ECS (Figure 6). The intensity, or flow velocity of the Kuroshio Current (KC) exhibits a summer maximum and a winter minimum. During the summer, the average flow velocity is approximately 0.9 m/s, with maximum velocities exceeding 1 m/s. In contrast, the average flow velocity during the winter is approximately 0.6 m/s. Additionally, during the summer, the main axis of the KC moves away from the continental slope of the ECS (Figure 6b), while during the winter, the surface seawater is invaded by a large volume of water from the ECS shelf under the influence of the northward monsoon (Figure 6d). The spring and autumn seasons show transitional states between the winter and summer conditions (Figure 6a,c). Similar to previous studies, the Taiwan Warm Current (TWC) flows northward throughout the year between the 50–100 m isobaths, but its northward intensity varies seasonally. During the summer, the TWC bifurcates around 28.5°N, with one branch turning eastward to merge with the KC, while the main branch continues northward to the mouth of the Changjiang River beyond 30°N (Figure 6b). In the winter, the TWC bifurcates around 27.5°N, with one branch merging with the KC, while the main branch continues northward to the eastern offshore of Zhoushan beyond 29°N before turning eastward (Figure 6d). The Changjiang's freshwater discharge converges with the continental shelf water mass behind its estuary and creates the Changjiang Diluted

Water (CDW), which subsequently flows northeastwards toward Jeju Island. During the spring and summer seasons, the CDW veers southeastwards beyond the 124°E , streaming toward the adjacent waters of the KC (Figure 6a,b). In autumn, the CDW maintains its eastward movement (Figure 6c), while in winter, it is swayed by the south branch of the Yellow Sea circulation system and the northward Yellow Sea warm current east of 125°E , compelling it to deflect northeastwards (Figure 6d). It is worth noting that during the winter, a branch of the CDW flows along the coastline southwards beyond its estuary (Figure 6d), forming the Zhe-Min Coastal Current, which moves in a southerly direction due to the influence of the northerly monsoon (although it may be difficult to observe using satellite imagery because of its proximity to the coastline). In addition, satellite observations have successfully identified the seasonal characteristics of the Zhejiang Coastal Current (ZJCC): during autumn, it flows southward under the influence of the north wind (Figure 6c), while in summer, it flows northward due to the impact of the south wind (Figure 6b).

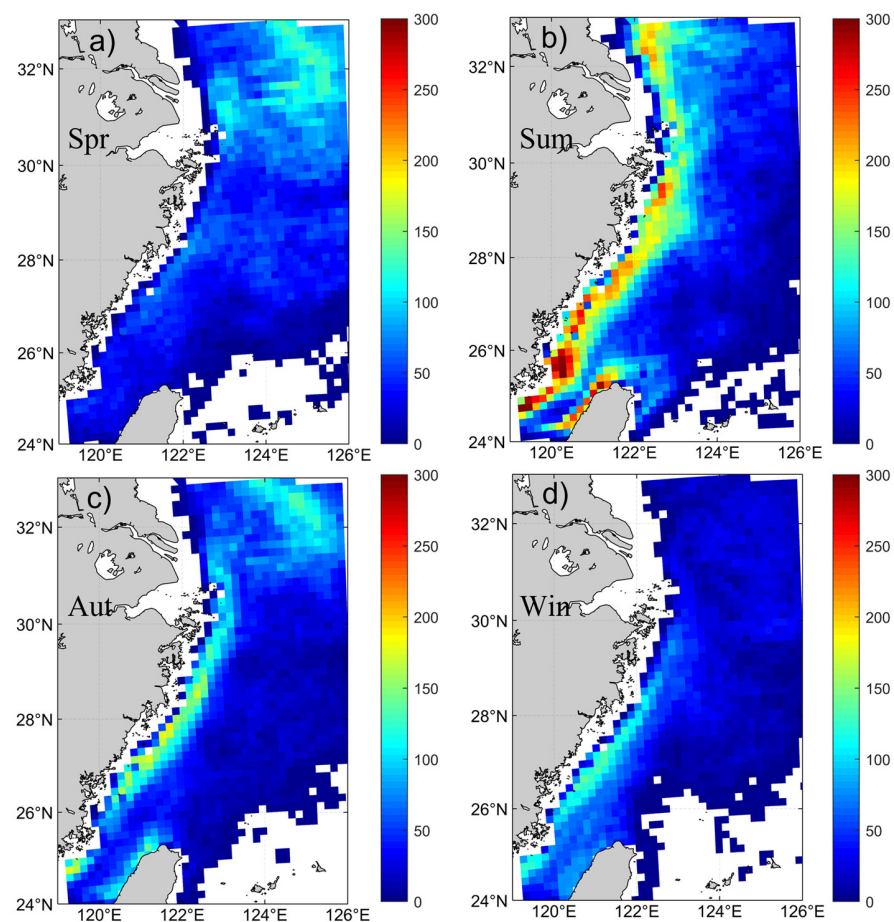


Figure 7. Seasonal distribution of the number of derived current vectors in the East China Sea. (a) Spring. (b) Summer. (c) Autumn. (d) Winter.

3.3. Diurnal Variability and Mechanisms of TSS in the Zhejiang Coastal Front

The Zhejiang Coastal Front (ZJCF), situated along the southeastern coast of China, serves as an intermediary zone between two oceanic currents—the nearshore Zhejiang Coastal Current (ZJCC), characterized by its low salinity and high turbidity, and the off-shore Taiwan Warm Current (TWC), known for its high salinity and low turbidity. Due to the barrier effect of the oceanfront, highly turbid nearshore water masses are restricted in their ability to be transported across the front, resulting in their accumulation primarily along the coastal areas. As coastal ocean development continues to grow, increasing attention is being paid to marine environmental issues. The distribution and variation in suspended sediments and pollutants in nearshore waters have become new critical

concerns in both physical oceanographic research and marine engineering projects. The transport, deposition, and resuspension of suspended sediments under the influence of ocean dynamics, such as ocean currents, waves, and monsoons, can cause changes in the topography of the seafloor. This, in turn, affects shoreline evolution, channel dredging, and the stability of underwater slopes. Moreover, fine particles of suspended sediment possess a strong adsorption capacity and often act as carriers of heavy metals, nitrogen, phosphorus, and other pollutants, influencing the accumulation and movement of contaminants in nearshore waters. Therefore, the distribution and variation in suspended sediments are an indispensable and integral component of sedimentation, material flux, and the physical environment of coastal waters. In this research, we initially chose a series of eight consecutive GOCI TSS satellite images captured on an unclouded day on 3 August 2013. Utilizing the 70 m isobath as the outermost boundary, we computed and scrutinized the intraday high-frequency changes in the spatially averaged TSS within the Zhejiang Coastal Front. Additionally, we conducted a diagnostic analysis of the underlying mechanisms of TSS variations based on the flow fields concurrently retrieved during the same period.

The results indicated that there is a diurnal variation in the spatial mean of surface TSS within the frontal zone along the coast of Zhejiang within the 70 m isobath (Figure 8h): an increasing trend from 8:00 to 12:00, followed by a decreasing trend from 12:00 to 15:00. The concurrently inverted surface current field is well correlated with the observed tidal elevation from the local tide gauge stations (Figure 8i), and it exhibits a primarily rotating tidal current pattern over time: from 8:00 to 12:00 (Figure 8a–d), the surface current field moves offshore, then, from 12:00 to 14:00 (Figure 8e–f), the current field changes to a northward alongshore flow, and from 14:00 to 15:00 (Figure 8g), the current field further shifts to an onshore direction. Indeed, as evident from Figure 8h, the alterations in TSS demonstrate a strong negative correlation with the alterations in tidal elevation, with a correlation coefficient of $R = -0.83$. This suggests that the alterations in TSS within the frontal zone along the coast of Zhejiang are predominantly influenced by the local tidal currents.

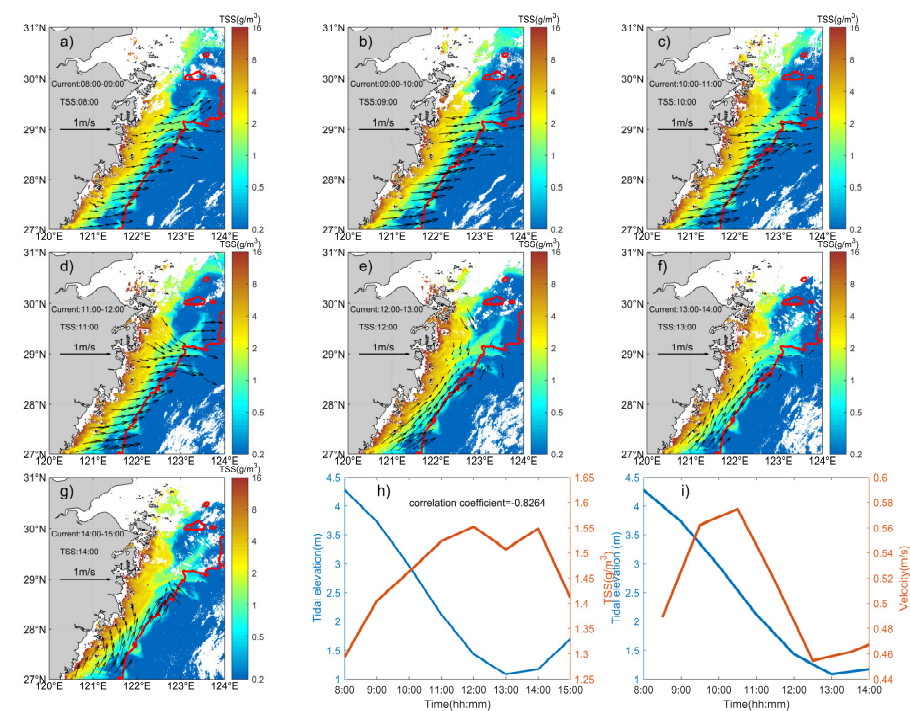


Figure 8. (a–g) Surface current field (red line represents the 70 m isobath); (h) tidal elevation observed from local tide gauge station (blue line) and spatially averaged TSS variation within 70 m isobath (red line); and (i) regional mean current velocity within 70 m isobath and tidal elevation from 8:00 to 14:00 on 3 August 2013.

The variations in surface TSS are usually accompanied by both vertical and horizontal dynamical processes. To elucidate the main physical processes governing variations in surface TSS in the front zone along the Zhejiang coast, we conducted a diagnostic analysis based on the advection-diffusion equation for TSS [25], which is given below:

$$\frac{\partial S}{\partial t} = V \cdot \nabla S - \nabla \cdot G + \Sigma, \quad G = (\overline{u'S'}, \overline{v'S'}) \quad (4)$$

where S is the TSS concentration; V is the surface horizontal flow velocity components u and v ; u' , v' , and S' represent anomalies of u , v , and S ; $G = (\overline{u'S'}, \overline{v'S'})$ is the diffusion flux vector in the horizontal direction; $V \cdot \nabla S$ is the horizontal advection term; $-\nabla \cdot G$ is the horizontal diffusion term; and Σ represents all of the other terms related to the vertical, namely the vertical convection term, the vertical diffusion term, and the settling term.

The diagnostic results (Figure 9) indicated that the magnitude for the hourly variations in TSS was 10^{-5} , while the magnitude for the advection term was 10^{-6} , the magnitude for the horizontal diffusion term was 10^{-7} , and the magnitude for the vertical processes was 10^{-5} . Thus, it can be inferred that the vertical processes, which involve vertical convective and diffusive transport of water masses, sediment settling, and resuspension, play a crucial role throughout the entire process of TSS changes. This is also evident from the degree of conformity between the two lines as they vary with time (The blue line and the purple line in Figure 9). In comparison to the contribution of vertical processes, the contribution of the diffusion term is almost negligible, while the contribution of the advection term is of the same order as that of the vertical processes only after 12:00. Figure 10 displays the spatial distribution of the absolute values of hourly variations in TSS, horizontal advection term, horizontal diffusion term, and vertical term from 10:00–11:00 and 11:00–12:00. It can be observed that the hourly variations in TSS exhibit a stable band-shaped distribution parallel to the coastline, with decreasing intensity offshore, indicating that water depth influences TSS changes. The distribution of horizontal advection and vertical terms is similar to that of hourly variations in TSS, and the intensity of the vertical term is greater than that of the horizontal advection term. The horizontal diffusion term is of the smallest magnitude and almost negligible. Thus, it is evident that vertical dynamic processes dominate the variations in surface TSS in the local area, with some contribution from horizontal advection, while the contribution from horizontal diffusion can be ignored.

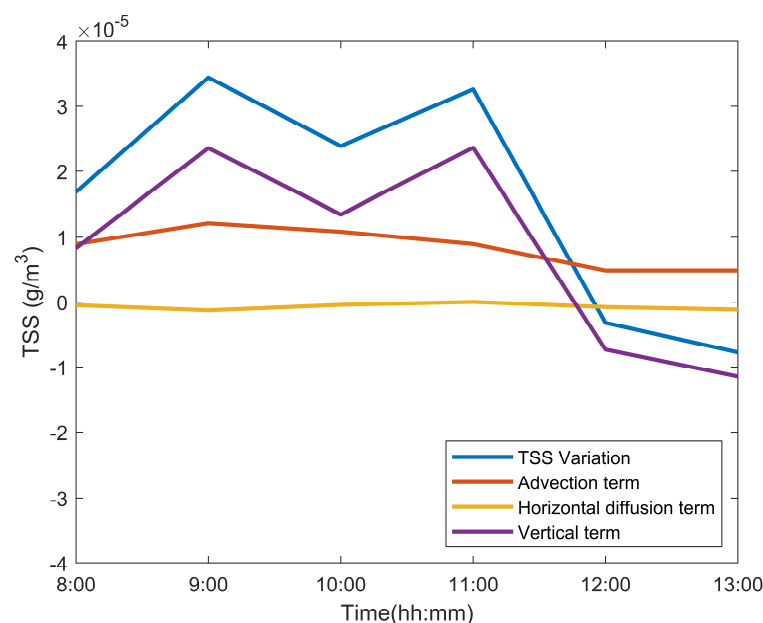


Figure 9. The hourly variation in TSS, advection term, horizontal diffusion term, and vertical term from 08:00 to 13:00 on 3 August 2013.

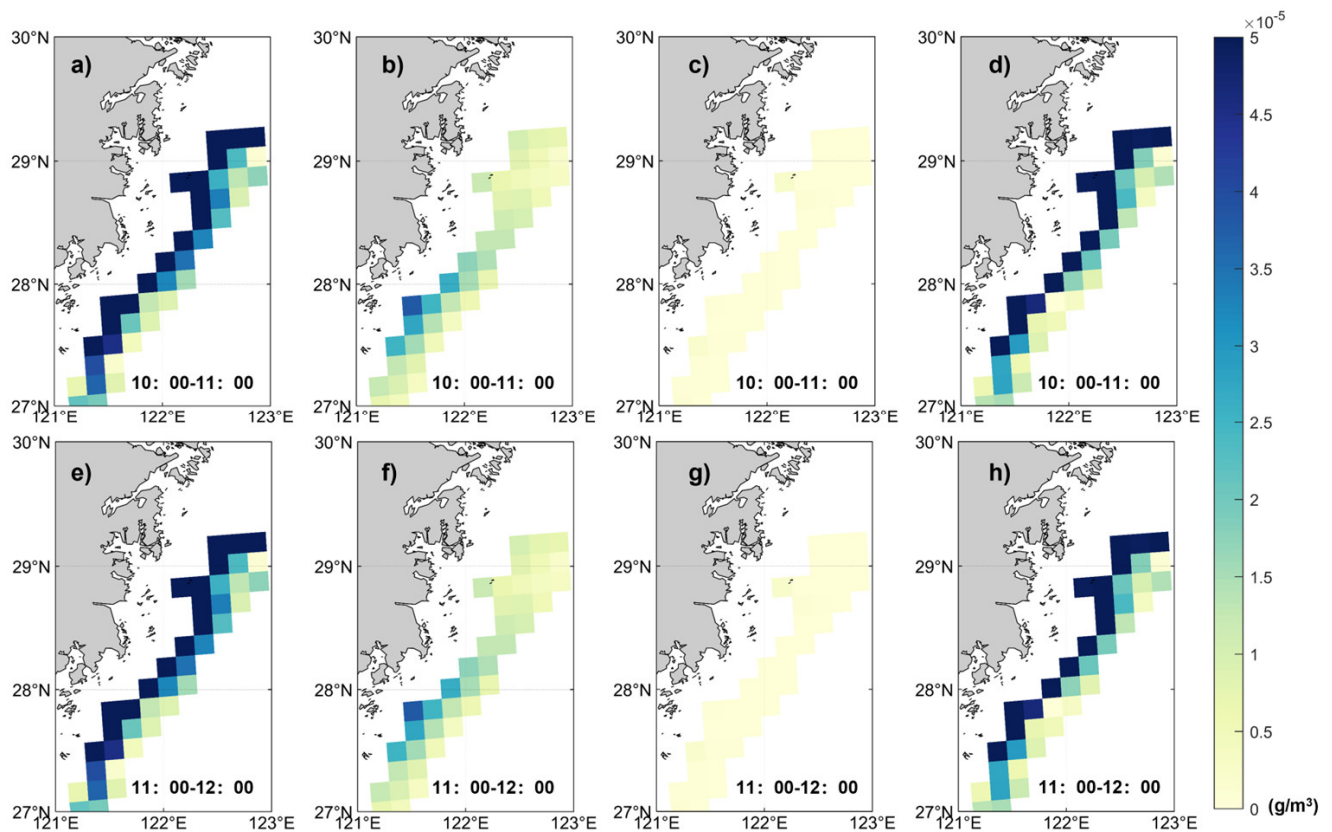


Figure 10. Spatial distribution of hourly variation in TSS, advection term, horizontal diffusion term, and vertical term at 10:00–11:00 (a–d) and 11:00–12:00 (e–h) on 3 August 2013.

The above analysis indicates that the vertical processes of water masses are the primary cause of the surface TSS variations along the Zhejiang Coastal Front. Previous research has suggested that short-term TSS variations near the East China Sea are dominated by bottom shear stress and tidal mixing [26,27]. As previously mentioned, the vertical term includes convective terms, vertical diffusion, sedimentation, and resuspension of sediments. In order to investigate how convective terms, i.e., tidal-induced mixing, affect TSS variations, we introduced the Simpson–Hunter index [28], which represents the stability of the seawater stratification: $k = \log \frac{H}{U^3}$, where H is the water depth, and $U = \sqrt{u^2 + v^2}$ is the surface horizontal velocity. A larger k value indicates greater seawater stratification stability and weaker vertical convection. Figure 11 reveals that during the early to mid-ebb tide period (8:00–12:00), there is a negative correlation between the TSS changes and k , with an increase in the TSS variation rate corresponding to a decrease in k . However, after 12:00, during the slack tide period, the TSS variations appear to be unrelated to tidal mixing. At this point, it is speculated that the vertical movement is mainly due to sedimentation and the resuspension of sediments. Furthermore, during the slow water flow rate of the slack tide stage, the slow movement of the water body implies a longer response time for sedimentation, which generally lags by approximately 2 h.

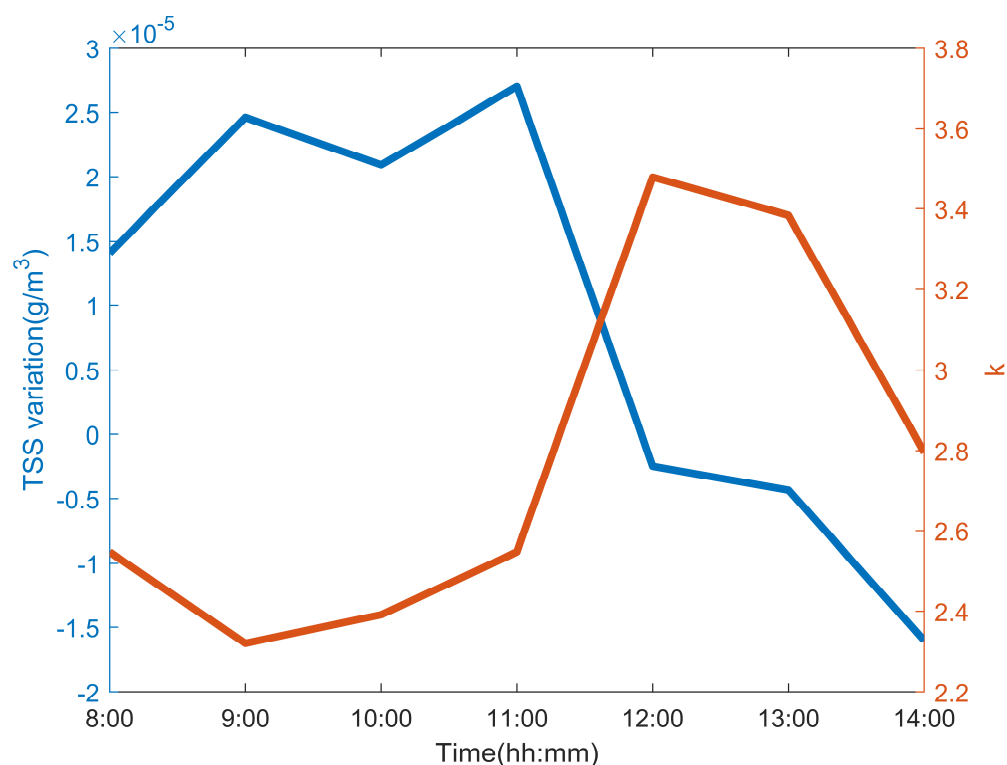


Figure 11. The evolution of Simpson–Hunter index k versus hourly variations in TSS from 8:00 to 14:00.

4. Conclusions

A geostationary satellite can track the movement of oceanic water masses through the continuous monitoring of tracers in the water, such as TSS or SST, thereby facilitating the inference of large-scale synchronized oceanic surface flow fields. This article employs the MCC algorithm to estimate the surface flow field of the East China Sea using continuous TSS imagery captured by the Korean geostationary ocean color satellite, GOCI. The spatial distribution of the inverted sea flow vector quantity revealed that cloud cover is the primary factor influencing the performance of the MCC algorithm, with a maximum quantity of inverted sea flow observed in summer and a minimum in winter. Furthermore, the number of sea flow vectors is higher in nearshore regions with high turbidity and lower in offshore regions with low turbidity, indicating that the movement of water masses with distinct characteristics and clear structures is more readily captured by the MCC algorithm. The spectrum analysis of the tide gauge station's tidal elevation shows that M_2 and S_2 semidiurnal tides are the main tidal components that dominate the dynamic processes in the East China Sea. Among them, the magnitude of M_2 is much larger than that of S_2 . The inversion results were compared with the modeled tidal current data and the measured tidal elevation data for verification. The results of the verification demonstrated that the mean deviation of the long semiaxis of the tidal ellipse of the inverted M_2 tide was 0.0335 m/s, the mean deviation of the short semiaxis was 0.0276 m/s, and the mean deviation of the tilt angle was 6.89° . Moreover, the spatially averaged flow velocity corresponded to the observed pattern of tidal elevation changes, thus showcasing the field's significant reliability.

The climate map of inversion flow fields lucidly delineates the spatial distribution of the surface circulation system in the East China Sea: The Kuroshio Current originates from the east coast of Taiwan, flows northeast along the continental slope, and finally reaches Japan; The Taiwan Warm Current enters the East China Sea shelf area through the Taiwan Strait and flows northward throughout the year; the Changjiang Diluted Water, carrying an enormous amount of sediment, flows into the East China Sea, initially turning northeast

and ultimately bending southeast. The seasonal distribution map of the inverted flow fields reveals the seasonal oscillations of the surface circulation in the East China Sea, revealing the following salient characteristics: (1) The surface Kuroshio Current displays a seasonal vigor disparity, with a robust presence during summer and a weakened manifestation in winter. During the summer season, the current moves away from the East China Sea shelf, while during winter, it penetrates extensively onto the shelf due to the Ekman transport caused by the northward monsoon. (2) Analogously, the Taiwan Warm Current exhibits a summer-dominant, winter-subdued trend, wherein it moves northward during summer under the influence of the southward monsoon, reaching the mouth of the Changjiang at a latitude beyond 30°N. In contrast, during winter, it encounters hindrances from the northward monsoon and deflects northeastward to merge with the Kuroshio Current, with a maximum extent of 29°N toward the north. (3) During summer, the Changjiang Diluted Water flows vigorously, and the outflow initially diverts northeast toward Jeju Island before turning southeast around 124°E. In winter, the flow of the Changjiang Diluted Water is relatively weak, with a portion flowing along the coastline toward the south (although this study was unable to successfully invert the data due to proximity to the shore), while another portion is carried northeastward by the southern branch of the Yellow Sea Current.

The variations in TSS within the frontal zone along the coast of Zhejiang are intricate, yet display notable tidal periodicity characteristics: an increasing trend from 8:00 to 12:00, followed by a decreasing trend from 12:00 to 15:00. According to diagnostic analysis based on inverted hourly flow field data, it is revealed that the intraday variation in local surface TSS was primarily influenced by tidally induced vertical mixing.

Frequent and precise measurements of surface current fields in real time are crucial for the advancement of physical oceanography research. This study serves to confirm the dependability of short-period surface flow inversion techniques for high-turbidity coastal waters utilizing geostationary satellites. The resultant inverted flow fields have a wide range of applications, including marine transportation, production, disaster mitigation, and rescue, among others. Moreover, when combined with additional data sources, these datasets can facilitate the analysis of relevant dynamic phenomena. Ultimately, this investigation's outcomes will enhance and augment our comprehension of the circulation structure and hydrodynamic environment of the Zhejiang offshore area, thereby providing a scientific foundation for both offshore environmental conservation and economic production activities.

Author Contributions: Conceptualization, W.Y.; methodology, Y.M. and W.Y.; software, Y.M.; validation, Y.M.; formal analysis, W.Y., Z.G. and J.X.; data curation, Y.M., Z.G. and J.X.; writing—original draft preparation, Y.M. and W.Y.; writing—review and editing, W.Y., Z.G. and J.X.; visualization, Y.M.; supervision, W.Y.; funding acquisition, W.Y. All authors have read and agreed to the published version of the manuscript.

Funding: This research was funded by the National Natural Science Foundation of China, grant number (41906025).

Data Availability Statement: The GOCI data used in this study can be downloaded from the KOSC website (<https://kosc.kiost.ac.kr/> accessed on 23 December 2021); the TPXO8 model tidal data can be downloaded from the website (<https://www.tpxo.net> accessed on 15 December 2022); and the FVCOM model data can be obtained from Xuan [16] for 2016.

Conflicts of Interest: The authors declare no conflict of interest.

References

1. Stabeno, P.; Reed, R. Circulation in the Bering Sea basin observed by satellite-tracked drifters: 1986–1993. *J. Phys. Oceanogr.* **1994**, *24*, 848–854. [[CrossRef](#)]
2. Barrick, D.E.; Evans, M.; Weber, B. Ocean Surface Currents Mapped by Radar: Mobile coastal units can map variable surface currents in real time to 70 kilometers, using ocean wave scatter. *Science* **1977**, *198*, 138–144. [[CrossRef](#)] [[PubMed](#)]
3. Durand, F.; Shankar, D.; Birol, F.; Sheno, S. Spatiotemporal structure of the East India Coastal Current from satellite altimetry. *J. Geophys. Res. Oceans* **2009**, *114*. [[CrossRef](#)]

4. Emery, W.J.; Thomas, A.; Collins, M.; Crawford, W.R.; Mackas, D. An objective method for computing advective surface velocities from sequential infrared satellite images. *J. Geophys. Res. Oceans* **1986**, *91*, 12865–12878. [[CrossRef](#)]
5. Tokmakian, R.; Strub, P.T.; McClean-Padman, J. Evaluation of the maximum cross-correlation method of estimating sea surface velocities from sequential satellite images. *J. Atmos. Ocean. Technol.* **1990**, *7*, 852–865. [[CrossRef](#)]
6. Bowen, M.M.; Emery, W.J.; Wilkin, J.L.; Tildesley, P.C.; Barton, I.J.; Knewton, R. Extracting multiyear surface currents from sequential thermal imagery using the maximum cross-correlation technique. *J. Atmos. Ocean. Technol.* **2002**, *19*, 1665–1676. [[CrossRef](#)]
7. Crocker, R.I.; Matthews, D.K.; Emery, W.J.; Baldwin, D.G. Computing Coastal Ocean Surface Currents From Infrared and Ocean Color Satellite Imagery. *IEEE Trans. Geosci. Remote Sens.* **2007**, *45*, 435–447. [[CrossRef](#)]
8. Yang, H.; Choi, J.-K.; Park, Y.-J.; Han, H.-J.; Ryu, J.-H. Application of the Geostationary Ocean Color Imager (GOCI) to estimates of ocean surface currents. *J. Geophys. Res. Oceans* **2014**, *119*, 3988–4000. [[CrossRef](#)]
9. Hu, Z.; Wang, D.P.; Pan, D.; He, X.; Miyazawa, Y.; Bai, Y.; Wang, D.; Gong, F. Mapping surface tidal currents and Changjiang plume in the East China Sea from Geostationary Ocean Color Imager. *J. Geophys. Res. Oceans* **2016**, *121*, 1563–1572. [[CrossRef](#)]
10. Taniguchi, N.; Kida, S.; Sakuno, Y.; Mutsuda, H.; Syamsudin, F. Short-Term Variation of the Surface Flow Pattern South of Lombok Strait Observed from the Himawari-8 Sea Surface Temperature. *Remote Sens.* **2019**, *11*, 1491. [[CrossRef](#)]
11. Zhu, Z.; Geng, X.; Li, S.; Xie, T.; Yan, X.-H. Ocean surface current retrieval at Hangzhou Bay from Himawari-8 sequential satellite images. *Sci. China Earth Sci.* **2020**, *63*, 1026–1038. [[CrossRef](#)]
12. Yin, W.; Huang, D. Evolution of submesoscale coastal frontal waves in the East China Sea based on geostationary ocean color imager observational data. *Geophys. Res. Lett.* **2016**, *43*, 9801–9809. [[CrossRef](#)]
13. He, S.; Huang, D.; Zeng, D. Double SST fronts observed from MODIS data in the East China Sea off the Zhejiang–Fujian coast, China. *J. Mar. Syst.* **2016**, *154*, 93–102. [[CrossRef](#)]
14. Choi, J.-K.; Park, Y.J.; Ahn, J.H.; Lim, H.-S.; Eom, J.; Ryu, J.-H. GOCI, the world’s first geostationary ocean color observation satellite, for the monitoring of temporal variability in coastal water turbidity. *J. Geophys. Res. Oceans* **2012**, *117*. [[CrossRef](#)]
15. Hu, Z.; Wang, D.-P.; He, X.; Li, M.; Wei, J.; Pan, D.; Bai, Y. Episodic surface intrusions in the Yellow Sea during relaxation of northerly winds. *J. Geophys. Res. Oceans* **2017**, *122*, 6533–6546. [[CrossRef](#)]
16. Xuan, J.; Yang, Z.; Huang, D.; Wang, T.; Zhou, F. Tidal residual current and its role in the mean flow on the Changjiang Bank. *J. Mar. Syst.* **2016**, *154*, 66–81. [[CrossRef](#)]
17. Stammer, D.; Ray, R.; Andersen, O.B.; Arbic, B.; Bosch, W.; Carrère, L.; Cheng, Y.; Chinn, D.; Dushaw, B.; Egbert, G. Accuracy assessment of global barotropic ocean tide models. *Rev. Geophys.* **2014**, *52*, 243–282. [[CrossRef](#)]
18. Liu, J.; Emery, W.J.; Wu, X.; Li, M.; Li, C.; Zhang, L. Computing Ocean Surface Currents From GOCI Ocean Color Satellite Imagery. *IEEE Trans. Geosci. Remote Sens.* **2017**, *55*, 7113–7125. [[CrossRef](#)]
19. Barton, I.J. Ocean currents from successive satellite images: The reciprocal filtering technique. *J. Atmos. Ocean. Technol.* **2002**, *19*, 1677–1689. [[CrossRef](#)]
20. Du, Y.; Xu, Q.; Cheng, Y.; Zhang, S.; Wang, C. Estimating Sea Surface Currents Based on Himawari-8 Sea Surface Temperature Data. In Proceedings of the 2021 Photonics & Electromagnetics Research Symposium (PIERS), Hangzhou, China, 21–25 November 2021; pp. 2034–2038.
21. Kagimoto, T.; Yamagata, T. Seasonal transport variations of the Kuroshio: An OGCM simulation. *J. Phys. Oceanogr.* **1997**, *27*, 403–418. [[CrossRef](#)]
22. Guan, B.X. A sketch of the current structures and eddy characteristics in the East China Sea. *Stud. Mar. Sin.* **1986**, *27*, 1–22.
23. Yu, H.; Zheng, D.; Jiang, J. Basic hydrographic characteristics of the studied area. In Proceedings of the International Symposium on Sedimentation on the Continental Shelf with Special Reference to the East China Sea, Hangzhou, China, 12–16 April 1983; pp. 295–305.
24. Warren, M.A.; Quartly, G.D.; Shutler, J.D.; Miller, P.I.; Yoshikawa, Y. Estimation of ocean surface currents from maximum cross correlation applied to GOCI geostationary satellite remote sensing data over the Tsushima (Korea) Straits. *J. Geophys. Res. Oceans* **2016**, *121*, 6993–7009. [[CrossRef](#)]
25. Zhou, Y.; Xuan, J.; Huang, D. Tidal variation of total suspended solids over the Yangtze Bank based on the geostationary ocean color imager. *Sci. China Earth Sci.* **2020**, *63*, 1381–1389. [[CrossRef](#)]
26. Hu, Z.; Pan, D.; He, X.; Bai, Y. Diurnal Variability of Turbidity Fronts Observed by Geostationary Satellite Ocean Color Remote Sensing. *Remote Sens.* **2016**, *8*, 147. [[CrossRef](#)]
27. Hu, Z.; Pan, D.; He, X.; Song, D.; Huang, N.; Bai, Y.; Xu, Y.; Wang, X.; Zhang, L.; Gong, F. Assessment of the MCC method to estimate sea surface currents in highly turbid coastal waters from GOCI. *Int. J. Remote Sens.* **2016**, *38*, 572–597. [[CrossRef](#)]
28. Simpson, J.; Hunter, J. Fronts in the Irish sea. *Nature* **1974**, *250*, 404–406. [[CrossRef](#)]

Disclaimer/Publisher’s Note: The statements, opinions and data contained in all publications are solely those of the individual author(s) and contributor(s) and not of MDPI and/or the editor(s). MDPI and/or the editor(s) disclaim responsibility for any injury to people or property resulting from any ideas, methods, instructions or products referred to in the content.